Acta Materialia 292 (2025) 121061

Contents lists available at ScienceDirect

Acta Materialia

journal homepage: www.elsevier.com/locate/actamat

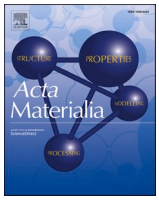

Full length article

Grain refinement of dual phase steel maximizes deformation ability of martensite, leading to simultaneous enhancement of strength and ductility

Myeong-heom Park [a,*], Akinobu Shibata [a,b], Stefanus Harjo [c], Nobuhiro Tsuji [a,d,*]

[a] Department of Materials Science and Engineering, Kyoto University, Yoshida Honmachi, Sakyo-ku, Kyoto 606-8501, Japan
[b] Research Center for Structural Materials, National Institute for Materials Science (NIMS), 1-2-1 Sengen, Tsukuba, 305-0047, Japan
[c] J-PARC Center, Japan Atomic Energy Agency, Naka-gun, Ibaraki 319-1195, Japan
[d] Elements Strategy Initiative for Structural Materials (ESISM), Kyoto University, Yoshida Honmachi, Sakyo-ku, Kyoto 606-8501, Japan

ARTICLE INFO

Keywords:
Strength-ductility synergy
Strain-hardening
Stress/strain partitioning
Deformation constraint
Digital image correlation (DIC)
In-situ neutron diffraction during deformation

ABSTRACT

Dual-phase (DP) steel, composed of soft ferrite and hard martensite, is well-known advanced high-strength steel (AHSS) because of its exceptional strength-ductility balance and low manufacturing cost. The present study found that microstructural refinement of DP steel enhanced not only its yield strength but also strain-hardening, leading to increasing both strength and ductility. Digital image correlation (DIC) analysis showed that strains were localized much more in soft ferrite than in hard martensite but the refinement of DP structure decreased the difference in average strains of ferrite and martensite, which avoided crack initiation in ferrite and led to large ductility. Consequently, the refinement of DP structure induced more plastic deformation in martensite through enhanced deformation constraints by the increase in ferrite/martensite interfaces. *In-situ* neutron diffraction experiment during tensile deformation quantitatively showed that higher phase stress was borne in hard martensite than in soft ferrite and microstructure refinement made martensite bear higher phase stress through the enhanced deformation constraint. Using strain/stress-partitioning results obtained by μ-DIC and *in-situ* neutron diffraction, individual stress-strain curves of ferrite and martensite could be successfully constructed for the first time. Individual stress-strain curves of ferrite and martensite reasonably explained the strength-ductility synergy in the fine-grained DP structure in terms of deformation constraint between two phases. Microstructure refinement in DP structures enhanced deformation constraint between two phases to maximize the deformation ability of martensite. The insight obtained in the present study could be applied to general heterostructured materials composed of soft and hard domains for overcoming the strength-ductility trade-off relationship.

1. Introduction

Dual-phase (DP) steels, composed of ferrite and martensite, are one of the most prominent class of steels widely used in automotive industries because of their excellent combination of strength and ductility, as well as low manufacturing cost. The well-balanced mechanical performance of DP steels is achieved through the cooperative deformation of ferrite and martensite, with playing a distinct role in plastic deformation. It has been considered that soft ferrite is primarily responsible for ductility, while hard martensite supports strength of DP steels. However, such understanding is too easy. In reality, DP steels usually have complex microstructures with different morphologies composed of ferrite and martensite. The microstructures include differences in fractions, strength (hardness), distributions and grain sizes of two phases (ferrite and martensite), all of which significantly affect the global mechanical properties of DP steels. It should be noted that two phases (ferrite and martensite) having different mechanical properties must cooperatively deform. To comprehensively understand the deformation nature of DP steels with such microstructures, it is imperative to examine local deformation features in microstructural scales. Recent reports have shown that the local deformation behavior greatly changes depending on phase distribution in DP steels [1–3]. DP structures with a chain-shaped distribution of martensite surrounding individual ferrite grains exhibited more homogeneous deformation compared to those with an isolated martensite distribution. The large ductility achieved in the chained DP could be attributed to the homogeneous deformation in its microstructure. Furthermore, it has been reported that grain refinement of DP steels enhances strength without a significant loss of

* Corresponding authors at: Department of Materials Science and Engineering, Kyoto University, Yoshida Honmachi, Sakyo-ku, Kyoto 606-8501, Japan.
E-mail addresses: park.myeongheom.8r@kyoto-u.ac.jp (M.-h. Park), nobuhiro-tsuji@mtl.kyoto-u.ac.jp (N. Tsuji).

https://doi.org/10.1016/j.actamat.2025.121061
Received 12 January 2025; Received in revised form 28 March 2025; Accepted 16 April 2025
Available online 16 April 2025

ductility, because of its enhanced strain-hardening ability [4–7]. However, the scientific origin of such a superior strain-hardening characteristic promoted by grain refinement in DP structures is still unclear. Enhanced strain-hardening ability by grain refinement is believed to be a unique feature of DP structure and also other types of hetero-structured materials, since in most cases single-phase metallic materials do not exhibit an increase in strain-hardening ability through grain refinement [8–13]. Thus, quantitatively characterizing deformation heterogeneity would be a key investigation for revealing the origin of high strain-hardening ability and the excellent strength-ductility balance given by the grain refinement in DP steels.

The present study uses micro-scale digital image correlation (μ-DIC) method and *in-situ* neutron diffraction during deformation for clarifying deformation behavior of DP steels composed of soft ferrite and hard martensite. The DIC method allows to measure local strains in ferrite and martensite regions separately [2,3,14,15], enabling to understand strain-partitioning behavior between ferrite and martensite in DP steels having different grain sizes. Stress-partitioning during deformation can be explored using the *in-situ* neutron diffraction experiment during deformation [16,17], which assesses the internal stresses (calculated from elastic strains) in ferrite and martensite phases. The combination of the DIC method and the *in-situ* neutron diffraction experiment would provide great synergy in understanding a full picture for the deformation roles of both phases in DP steels. The deformation role of each constituent phase and the scientific origin of outstanding mechanical properties achieved by the grain refinement in the DP steel are discussed based on obtained strain- and stress-partitioning results in the present study.

2. Experimental procedures

2.1. Microstructure fabrication

The material used in this study was a low-carbon steel with a chemical composition of Fe-2Mn-0.1C (Mn: 2.0, C: 0.103, Si: 0.01, P: <0.002, S: 0.0008, Fe: Balanced; mass %). The A_{e3} temperature, which is the lowest ortho-equilibrium temperature of austenite single-phase region, was calculated to be 804 °C using Thermo-Calc software with TCFE7.0 thermodynamic database applicable to Fe-based alloys. Fig. 1 illustrates two kinds of heat treatment routes designed to obtain ferrite-martensite dual-phase (DP) structures with different grain sizes. In the Route (1), the samples were austenitized at 950 °C or 830 °C for 6hr for obtaining different grain sizes of austenite, followed by furnace cooling resulting in ferrite and (small amount of) pearlite structures with different grain sizes of pro-eutectoid ferrite. Subsequently, the samples were intercritically annealed at 740 °C for 30 min and water-quenched to obtain ferrite-martensite DP structures. In the Route (2), which was designed to furthermore refine the ferrite grain size, the samples were heat-treated at 830 °C for 6hr and then water-quenched to obtain a fully martensitic structure. This material was followed by four-cycles of heat treatment with quick heating at 810 °C (just above A_{e3}) for 3 min and water quenching per each cycle, aiming to refine austenite grain size [18–20]. In the final 4th cycle, air cooling was carried out from 810 °C to obtain a fine-grained ferrite and pearlite structure. The specimens were then intercritically annealed in ferrite + austenite two-phase region in the phase diagram at 740 °C for 30 min, followed by water quenching to obtain a grain-refined DP structure. The details of the grain-refinement process through the cyclic heat treatment can be found in previous studies [18–20]. In both Route (1) and Route (2), austenite tends to form along grain boundaries of pro-eutectoid ferrite in intercritical annealing, so that DP structures with network-shaped martensite surrounding (pro-eutectoid) ferrite are obtained. Coarse-grained and medium-grained DP structures were obtained using the Route (1) with the austenitizing temperatures of 950 °C and 830 °C, respectively. A fine-grained DP structure was obtained through the Route (2).

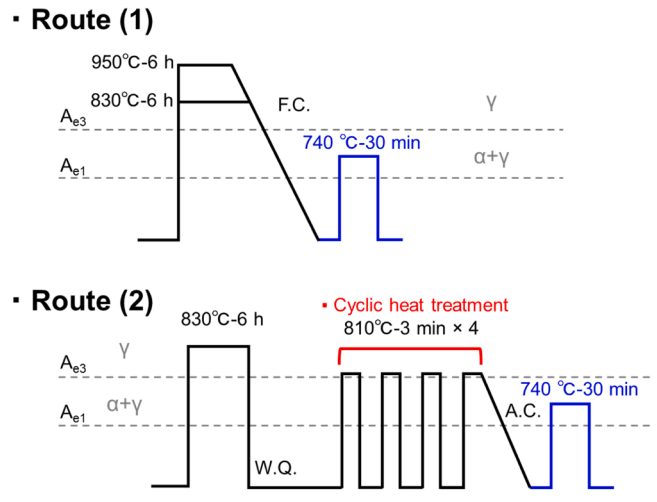

Fig. 1. Two different heat treatment routes for fabricating ferrite-martensite DP structures with different grain sizes of ferrite. A ferrite-pearlite structure was first obtained as the base structure in the present low-carbon steel, followed by the fabrication of the ferrite-martensite DP structures. In the Route (1), ferrite grain size was controlled by applying different austenitization temperatures (950 °C and 830 °C). In the route (2), further grain refinement of ferrite grains was achieved through the four-cycle heat treatment process. Both routes were finalized with intercritical annealing at 740 °C to obtain ferrite-martensite DP structures.

2.2. Microstructure observations

Microstructures of specimens were observed by a field-emission scanning electron microscope (SEM: JSM-7100, JEOL) equipped with electron backscattering diffraction (EBSD), operated at an accelerating voltage of 15 kV. The data of EBSD were collected using TSL Solutions software (TSL-OIM data collection, ver. 5.31) and used for the identification of crystal orientations and phases. The samples for SEM observations were prepared by mechanical polishing followed by electropolishing in a solution of 10 % $HClO_4$ and 90 % CH_3COOH at a voltage of 22 V for 30 s at room temperature. Average ferrite grain sizes were measured by the line intercept method on SEM microstructures, while block sizes of lath martensite were measured using the same method on EBSD orientation maps. The volume fraction of martensite was estimated by pixel counting in martensite regions on EBSD maps. Phase identification of ferrite and martensite was performed based on contrast differences in the EBSD image quality (IQ) maps, because martensite phase having fine substructures and high density of dislocations showed lower IQ values. The phase identification of austenite was conducted using the EBSD phase map.

2.3. Nano-indentation testing

The hardness (strength) of ferrite or martensite was investigated using a nanoindentation test (TI 950 TriboIndenter, Hysitron Inc.) under a constant load condition of 350 μN. A Berkovich nano-indenter, with a tip-central axis angle of 65.3° relative to each plane, was used. The tip had a base diagonal length of 7.52 μm and a height of 1 μm. Under these conditions, clear indents were observed, with lengths of approximately 0.3 μm for ferrite and 0.19 μm for martensite in the DP microstructure. Scanning probe microscope (SPM) images were obtained for each specimen by scanning the surface height. To ensure statistical reliability, the hardness test was performed at >300 points for each DP specimen. The indented regions were further examined in SEM to accurately identify the phases at each indented point. Points located on the boundaries were excluded from the hardness calculations.

2.4. Tensile properties and deformation behavior by digital image correlation (DIC) method

Mechanical properties of the DP structures were evaluated using a uniaxial tensile testing machine (AG-100 kN Xplus, SHIMADZU) with an initial strain rate of 8.3×10^{-4} s^{-1} at room temperature. The sheet-type tensile specimens with a 1/5 miniaturized size (10 mm gauge length, 5 mm width and 1 mm thickness) of the JIS (Japan Industrial Standard)-5 specimen were cut using an electrical wire-cutting machine (HS-70A, BROTHER). Before testing, the tensile specimens were speckle-patterned using black and white inks for precise strain analysis through the digital image correlation (DIC) technique, using a dedicated DIC strain-visualizing software (Vic-2D, Correlated solutions). During the tensile tests, digital images of the speckle-patterned tensile specimens were captured sequentially at a constant rate of 5 frames per second with a CCD camera. These images were processed for the DIC-strain analysis. Global tensile strain was measured precisely using the virtual extensometer function in the DIC software. Tensile tests were repeated at least two or three times for each condition to ensure the reproducibility of the results.

For local strain analysis in microstructures, microscopic DIC (μ-DIC) was performed using SEM microstructures taken before and after the tensile deformation to specific global strains. The small-sized tensile specimen used for the μ-DIC in SEM had a gauge length of 5 mm, width of 2.5 mm, and thickness of 1 mm. The contrast of SEM microstructures was used as the base pattern for μ-DIC strain analysis, and a grid pattern was additionally introduced on the surfaces of the tensile specimens using a focused ion beam (FIB) in order to enhance the accuracy of the μ-DIC analysis, even in the heavily deformed state. SEM images were captured at a resolution of 1280 × 1024 pixels, and DIC analyses were performed using nearly consistent subset settings. The subset size and inspection step were set to 49 pixels and 4 pixels for coarse-grained (CG) and fine-grained (FG) DP specimens, while those for medium-grained (MG) DP specimen were set to 57 pixels and 4 pixels. Strain measurements were conducted at each FIB-grid intersection, where the phase at each intersection was identified based on SEM contrast and morphological characteristics. Strains at the interfacial boundaries were excluded from the analysis in the present study, as they reflect the mixed properties of ferrite and martensite, which can vary depending on the boundary inclination in the thickness direction.

2.5. In-situ neutron diffraction study during tensile deformation

In-situ neutron diffraction experiment was conducted to measure the elastic strain and internal stress of each phase during tensile deformation, performed at the J-PARC (Japan Proton Accelerator Research Complex) MLF (Materials and Life Science Experimental Facility) Beam line-19 TAKUMI. Double hook-type tensile specimens with gauge dimensions of 12 mm length × 3 mm width × 1.5 mm thickness were used for the analysis. The tensile testing was carried out at an initial strain rate of 8.3×10^{-4} s^{-1} at room temperature. The deformation was interrupted at various tensile strains, with each interruption held for 20 min to collect statistically reliable diffraction peak profiles for each deformation state. The tensile loading axis was aligned at a tilting angle of ± 45° relative to the direction of the two detectors set on the different sides of the specimen. The white neutron beam with various wavelengths was projected to the specimen in the direction 45° relative to the tensile loading axis. This specific setup enabled two detectors to selectively collect peak profiles for all (hkl) planes perpendicular and parallel to the tensile direction, respectively. Peak fitting, using a mixed Gaussian and Lorentzian function, was applied to separate the ferrite and martensite phases from the overlapped diffraction peaks of ferrite (with BCC crystal structure) and martensite (BCT). Lattice elastic strain on (110) plane perpendicular to the tensile axis (e^{110}) is defined as $(d^{110}- d_0^{110})/ d_0^{110}$, where d_0^{110} and d^{110} indicate d-spacings before and during deformation, respectively. Using the obtained lattice elastic strain for ferrite or martensite, the internal stress of each phase (will be referred to as the phase stress) was estimated by employing the (110)-corresponding elastic constant (E^{110}) of 232 GPa, according to one-dimensional Hooke's law ($\sigma = E^{110}\ e^{110}$). This elastic constant was obtained through rotation-operation of elastic stiffness tensor in α-Fe with a $C_{1111} = 242$ GPa, $C_{1122} = 147$ GPa, and $C_{1212} = 112$ GPa (according to Fig. S1 in supplementary materials) under the assumption of random texture. The obtained elastic modulus was in good agreement with the elastic constant reported in the previous result [21] and also with the experimentally observed elastic slope in the applied stress-lattice elastic strain plots during elastic deformation in the present experiment. The same stress estimation process was applied to the (200) plane. Although the lattice elastic strain for the (200) plane was larger than that for the (110) plane, no significant difference in phase stress was observed, due to the much lower elastic constant for the (200) plane (130.9 GPa).

3. Results and discussions

3.1. Fabrication of DP structures with different grain sizes and their hardness properties

Fig. 2(a) shows EBSD-image quality (IQ) maps obtained from the different heat treatment routes. The ferrite and martensite phases were distinguished based on contrast differences in the IQ map. Martensite, characterized by higher density of lattice defects, appeared as darker contrast than ferrite. The ferrite grain sizes of the specimens obtained through the Route (1) shown in Fig. 1 with austenitizing temperatures of 950 °C and 830 °C were measured to be 58.3 μm, 8.2 μm, respectively. For the DP specimen obtained through the Route (2) in Fig. 1, the ferrite grain size was 4.1 μm. The martensite block size, which represented the effective grain size of martensite corresponding to its strength [19,20], was 1.01 μm, 0.84 μm and 0.65 μm, respectively. All the specimens exhibited similar martensite fractions of approximately 43 %. The martensite phase in all the specimens exhibited a chain-like (network) morphology surrounding individual ferrite grains. The presence of austenite and the texture were also characterized, as shown in Fig. S2 of the supplementary materials. No retained austenite phase was detected in any specimens, and all exhibited a relatively weak texture. Although the coarse-grained (58.3 μm) specimen showed some strong intensities in the (001) pole figure in Fig. S2, this could be attributed to the limited number of ferrite grains analyzed (only 17 ferrite grains included in the EBSD-analyzed region for the coarse-grained specimen).

Fig. 2(b) displays the nano-hardness result for each phase obtained from nano-indentation testing. The hardness values are mapped with different colors on the scanning probe microscope (SPM) images. The average hardness of ferrite in the DP specimens with the average ferrite grain sizes of 58.3 μm, 8.2 μm and 4.1 μm was 4.25 ± 0.69 GPa, 4.01 ± 0.39 GPa, and 4.11 ± 0.69 GPa, respectively, while the average hardness of martensite was 7.92 ± 1.86 GPa, 7.85 ± 1.27 GPa and 8.49 ± 1.78 GPa, respectively. This indicates that the hardness of two phases does not significantly vary with ferrite grain size. Although the hardness values in martensite showed some scatter, this was likely due to the complex microstructural features of lath martensite, which exhibited variations in orientation and dislocation distributions even within a single prior-austenite grain [22–24]. Based on the microstructural observations and the nano-hardness tests, it can be concluded that the main difference among the specimens is only the ferrite grain size. Hereafter, the specimens with the average ferrite grain sizes of 58.3 μm, 8.2 μm and 4.1 μm are referred to as the coarse-grained (CG), medium-grained (MG) and fine-grained (FG) specimens, respectively.

3.2. Tensile properties

Fig. 3(a) shows engineering stress-strain (S-S) curves for the DP specimens with different grain sizes of ferrite. The circle symbol on each S-S curve indicates the point corresponding to the uniform elongation. It

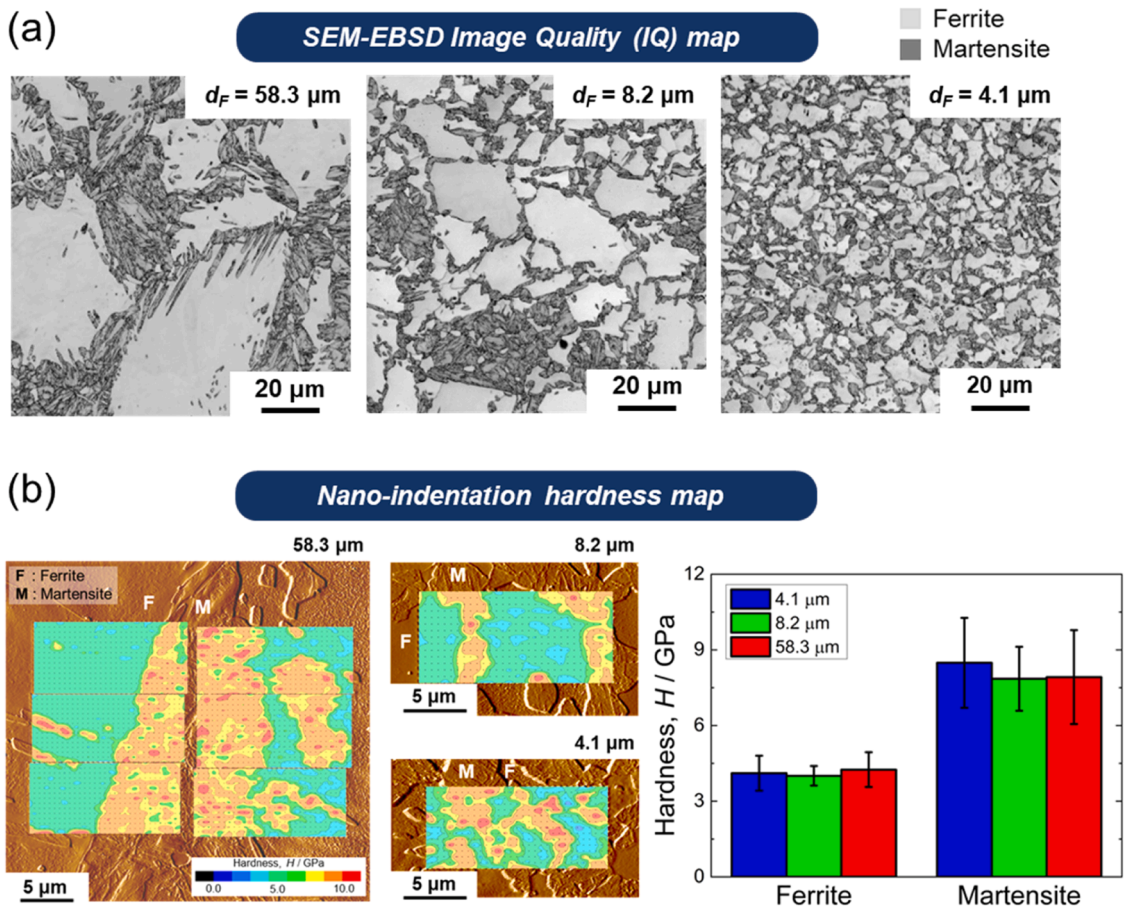

Fig. 2. Microstructures and nano-hardness properties of the low-carbon ferrite-martensite dual-phase (DP) steel specimens with average ferrite grain sizes of 58.3 μm, 8.2 μm and 4.1 μm. (a) SEM-EBSD image quality (IQ) maps of the DP specimens displaying the microstructures of different grin sizes. In the IQ map, martensite appears darker than ferrite due to its higher lattice defect density. (b) Nano-indentation hardness color maps overlapped on SPM (scanning probe microscopy) images of the identical regions, illustrating hardness distributions in ferrite and martensite. The graph on the right-hand side shows the average nano-hardness values of the two phases.

should be emphasized that the grain refinement simultaneously enhanced both strength and ductility. The FG specimen (4.1 μm) demonstrated a high ultimate tensile strength (UTS) of 896 MPa and a large total elongation of 0.219 (21.9 %), whereas the CG specimen (58.3 μm) showed a low UTS of 712 MPa and a small total elongation of 0.155 (15.5 %). All specimens displayed nearly the same uniform elongation (approximately 0.09 (9 %)). In contrast, the post-uniform elongation (elongation from the onset of macroscopic necking to tensile fracture) was significantly improved with the grain refinement. This indicates that the large ductility achieved by the grain refinement is primarily attributed to the enhanced post-uniform elongation.

The uniform elongation of materials can be discussed in terms of the plastic instability condition. According to the Considère criterion [25], the onset of plastic instability (start of macroscopic necking) is determined by the intersection of the strain-hardening rate ($d\sigma/d\varepsilon$) curve with the true stress-strain (σ-ε) curve. Fig. 3(b) shows the true stress-strain curves and the strain-hardening rate curves of the DP steel specimens with three different average ferrite grain sizes. The FG specimen demonstrated higher strain-hardening rate throughout the deformation, leading to the intersection at a greater strain. Such improved strain-hardening ability in the FG specimen contributed to its large uniform elongation in spite of its higher strength.

To explore the enhanced post-uniform elongation achieved through the grain refinement, Fig. 4(a) shows local strain distributions in the tensile specimens obtained from the DIC technique. The tensile axis is oriented vertically in the images, and the colors superimposed on the tensile specimens represent the von-Mises equivalent strain (ε_{eq}) at local points, of which strain values are expressed according to the strain color bar. Up to a global engineering strain of 8 %, all the tensile specimens exhibited mostly homogeneous deformation characterized by uniform color distributions in the local strain maps. At an engineering strain of 15.5 %, the CG specimen exhibited pronounced strain localization showing macroscopic necking, whereas the MG and FG specimens displayed less strain localization, indicating that the grain refinement delayed the onset of necking. At a strain of 20 %, both the MG and FG specimens showed necking with local strains exceeding 0.4, while the CG specimen already fractured.

For further analysis, the local strain (ε_{eq}^{Local}) at the highest strain point in the necked region was tracked as a function of the global engineering strain (e) throughout the tensile deformation until fracture (Fig. 4(b)). The black line in Fig. 4(b) represents ideal homogeneous deformation described as $\varepsilon_{eq}^{Local} = \varepsilon^{Global}$ (=ln(1 + e)). Initially, the local strain, ε_{eq}^{Local}, increased linearly along the homogeneous deformation line up to an engineering strain of 8 % for all the specimens. Then, ε_{eq}^{Local} showed a positive deviation from the line in all the specimens, indicating the occurrence of necking. As the grain size decreased, the increasing rate of ε_{eq}^{Local} became slower, but eventually reached higher strain values just before fracture. Thus, the significant post-uniform elongation observed in the FG specimen seems to be attributed to its gradual strain localization and the ability to endure high local strain prior to the fracture. Such notable differences in the strain localization behavior depending on the grain size can be furthermore examined by characterizing deformation behavior in microscopic scales, emphasizing the respective roles of ferrite and martensite phases during the deformation in the next

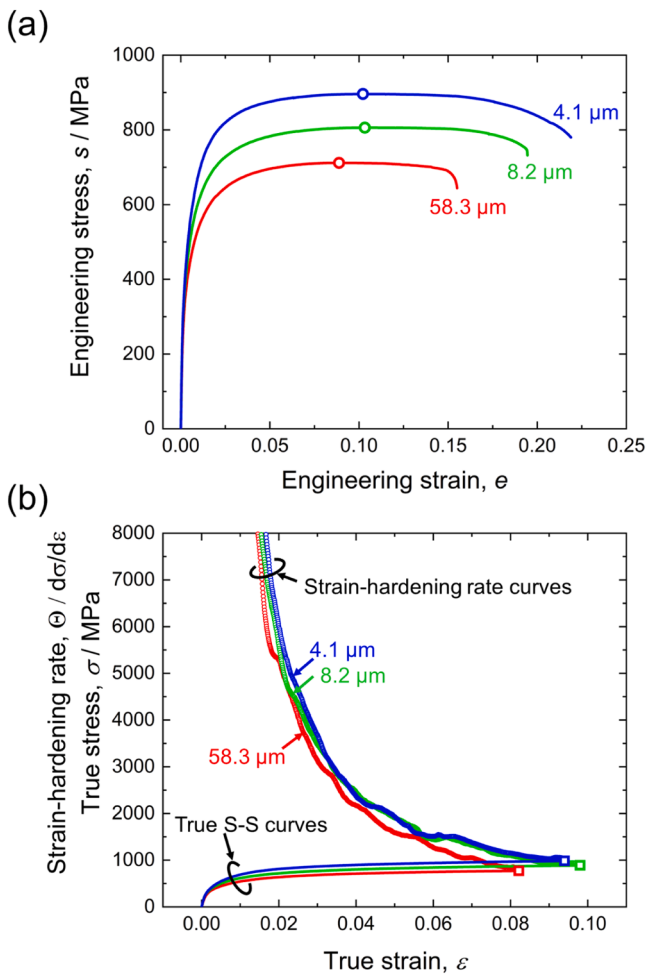

Fig. 3. (a) Engineering stress-strain curves of the DP specimens with different ferrite grain sizes, obtained from uniaxial tensile testing at room temperature under a quasi-static initial strain rate of 8.3×10^{-4} s^{-1}. The circle symbol on the graph represents the point of uniform elongation. (b) Strain-hardening rate curves and true stress-strain curves of the DP specimens. The square symbol denotes the crossing point of the strain-hardening rate with the true S-S curves, corresponding to the onset of plastic instability.

section.

3.3. Local strain distributions in microstructures

In order to analyze local strain distributions corresponding to microstructures and to quantify the average strain borne by ferrite or martensite phase, the μ-DIC technique was applied to the DP specimens having different average grain sizes of ferrite. Fig. 5 shows local strain distributions overlapped on the DP microstructures (left and middle columns) and corresponding strain histograms (right column) for the (a) CG, (b) MG and (c) FG specimens tensile deformed to an engineering strain of ~7.5 %. The middle column exhibits enlarged local strain maps of the regions surrounded by dotted white rectangles on the maps in the left column. Ferrite and martensite are labeled as **F** and **M** on the maps of the middle column, respectively, and the colors on the maps represent von-Mises equivalent strain values according to the color bar shown at the bottom of Fig. 5. White solid lines on the enlarged strain maps of the middle column indicate ferrite/martensite boundaries. The morphology of local strain distributions was similar in all the specimens. The regions with higher local strains located in softer ferrite phase and the strain concentrated regions aligned with inclinations of about 45° to the tensile direction. On the other hand, the DP specimens exhibited important differences in the strain distribution depending on the grain size, despite being subjected to nearly the same global strain condition ($e = 7.3$ % for CG, $e = 7.7$ % for MG and $e = 7.8$ % for FG). The strain histogram on the right column showed that the soft ferrite took higher strains than the hard martensite. However, the grain refinement significantly reduced strains within ferrite phase, which resulted from the fact that harder martensite could take larger plastic deformation. In other words, the strain distributions in ferrite and martensite became more homogeneous in the DP microstructures with finer grain sizes.

From the results of the local strain analysis by μ-DIC, like those shown in Fig. 5, for the specimens tensile-deformed to different strains, we could get average strains within each phase (i.e., ferrite or martensite). The evolution of strain distributions for the CG, MG and FG specimens is shown in Fig. S3 in the supplementary materials. In Fig. 6, the average strains within ferrite or martensite phase (the phase strain, hereafter) are plotted as a function of the average strain in the region mapped by μ-DIC, covering a wide global tensile strain range: from 0 % to 11.8 % for the CG specimen, 15.2 % for the MG specimen, and 15.3 % for FG specimen. Within the uniform elongation range (approximately 9 % engineering strain), the average strains of the mapped region (horizontal axis of the graph) matched well with the global tensile strains applied to the specimens. The homogeneous deformation in case of $\varepsilon^{F\ or\ M} = \varepsilon^{ave}$ is expressed by the black straight line in Fig. 6. The phase strains of both ferrite and martensite increased monotonically with tensile deformation, following a linear trend. The ferrite phase exhibited higher strains than the martensite phase throughout the tensile deformation process, which clearly indicated strain-partitioning between soft ferrite and hard martensite. It is noteworthy, however, that the difference in the phase strains between ferrite and martensite significantly decreased with the grain refinement. This means that the grain refinement makes the deformation of the DP steel with microstructures composed of soft and hard domains more homogeneous, which would contribute to the synergetic increase of both strength and ductility shown in Fig. 3. Figs. 5 and 6 clearly showed that the deformation in the DP steel composed of soft ferrite and hard martensite was naturally heterogeneous and concentrated in soft ferrite phase, but the deformation within two different phases became more homogeneous with the grain refinement. For quantitatively understanding the deformation heterogeneity/homogeneity in more detail, the μ-DIC results for the CG and FG specimens are compared next.

The upper image in Fig. 7 shows a local strain distribution overlapped on the microstructure in the CG specimen (average ferrite grain size of 58.3 μm) tensile deformed to about 12 % of global engineering strain. The profile of local strains along the yellow dotted line in the upper image of the CG specimen is plotted in red color as a function of distance in the lower graph. Along the 0.5 mm (500 μm) distance, the profile (red curve) showed the heterogeneous and somehow periodic distribution of local strains where large deformation was localized in ferrite regions. Such a localized deformation was also observed in the FG specimen (average ferrite grain size of 4.1 μm) deformed to about 12 % of global tensile strain, as shown in Fig. 5(c) and the middle images of Fig. 7. When the local strain profiles in four different regions of the FG specimen were plotted in the same scale (blue curve in the lower graph of Fig. 7), the profiles were greatly different from that of the CG specimen (red curve). The local strain profile in the FG specimen exhibited smaller amplitude and frequency than those in the CG specimen. The CG specimen showed the significant strain localization in which the maximum local strain reached 0.8, occurring in long-distance intervals (red curve in the lower graph in Fig. 7). Large micro-cracks approximately 20 μm in length were observed in the strain-localized regions, indicated by the white arrows on the strain map. In contrast, the local strain profile of the FG specimen (blue curve in the lower graph in Fig. 7) showed smaller maximum strain <0.4 and shorter frequency. No microcrack was observed in the microstructure of the FG specimen. The results of Fig. 7 confirmed that the deformation in the FG specimen was more homogeneous than that in the CG specimen. It can be concluded,

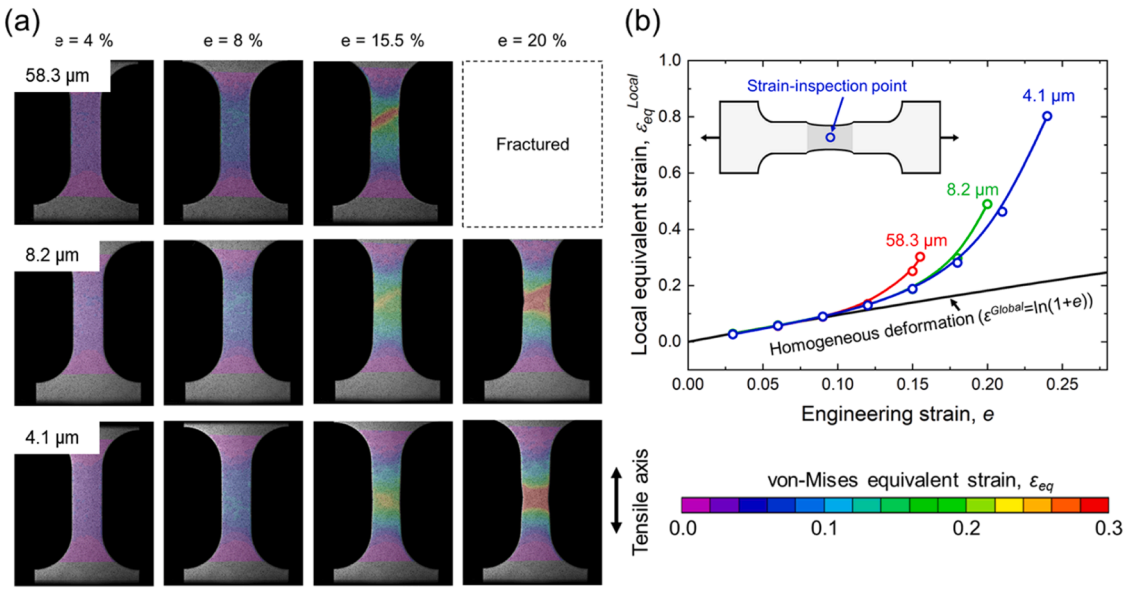

Fig. 4. Local strain evolution in the tensile specimens during deformation, evaluated by digital image correlation (DIC) technique. (a) DIC-local strain distribution maps in the tensile specimens with the average ferrite grain sizes of 58.3 μm, 8.2 μm and 4.1 μm at global engineering strain (e) of 4 %, 8 %, 15.5 % and 20 %. The tensile axis is parallel to the vertical direction in the images, and the color-coded map represents von-Mises equivalent strain values at local positions according to the provided strain color bar. (b) The highest local equivalent strain (ε_{eq}^{Local}) in the necked region plotted as a function of the global engineering strain (e). The data points (ε_{eq}^{Local}) correspond to the most strain-localized positions identified just before tensile failure. The black line indicates the ideal homogeneous deformation ($\varepsilon_{eq}^{Local} = \varepsilon^{Global}$ (=ln(1 + e))).

therefore, that the smaller tensile ductility of the CG specimen is due to the larger strain localization within the DP microstructure composed of soft (ferrite) and hard (martensite) phases accompanied with critical micro-cracks leading to failure, while the larger tensile ductility of the FG specimen is explained by the more homogeneous deformation within the DP structure.

3.4. *Internal stress evolution of ferrite and martensite*

In the previous sections, deformation of the DP steel specimens having different ferrite grain sizes was quantitatively analyzed from a viewpoint of strain by the use of the μ-DIC analysis. The difference in the tensile ductility (total elongation) between the CG and FG specimens could be understood from the degree of heterogeneity in strains between two specimens which was revealed by the local strain profiles obtained by the μ-DIC analysis. However, the mechanism about the effect of the grain refinement on the strength, uniform elongation and strain-hardening ability of the DP specimens remains unclear. This issue was examined by the use of the *in-situ* neutron diffraction during tensile deformation, which can provide insights on the internal stress evolution in each phase. Fig. 8(a) presents a schematic illustration of the setup for the *in-situ* neutron diffraction experiment at J-PARC MLF BL19 TAKUMI, together with the observed peak profiles of the fine-grained (FG) DP steel specimen having the average ferrite grain size of 4.1 μm, captured before (yellow) and during (black) deformation at an applied stress of 771 MPa. The diffraction data were obtained by the detector 1, so that the diffraction came from crystallographic planes perpendicular to the tensile direction. Diffraction peaks from the (110) plane perpendicular to the tensile axis were selected for the stress estimation owing to its strong peak intensity. Note that the observed (110) peak of BCC involves two peaks corresponding to ferrite and martensite, as both phases have body-centered cubic (bcc) structure (exactly speaking, martensite has body-centered tetragonal (BCT) structure) with a slight difference in d-spacing because martensite is a supersaturated solid solution of carbon [26,27]. During the tensile deformation, notable changes in both peak position and peak shape of (110) were observed (Fig. 8(b)). The peak position of the (110) diffraction peak shifted to the right, indicating an increase in the d-spacing of the (110) plane along the tensile loading axis, corresponding to elastic deformation. Moreover, the peak shape changed from symmetric to asymmetric during deformation. This transition suggested that ferrite and martensite exhibited different amounts of peak shifting, reflecting the differences in their elastic strains (stresses) under deformation. Results of the peak fitting for ferrite (red profile) and martensite (blue profile) shown in Fig. 8(b) revealed that martensite underwent a more pronounced peak shift during deformation, indicating plastically hard martensite bore larger elastic deformation than plastically soft ferrite.

Fig. 9 shows the change in the phase stress (the stress borne by each phase) of ferrite and martensite calculated using the lattice elastic strain of two phases obtained from the peak shift, as a function of the applied stress (global engineering stress). The black dashed line on the graph represents the isostress line for the two kinds of stresses, which serves as a reference for evaluating the degree of stress-partitioning. In the beginning of tensile deformation, the phase stress of ferrite and martensite lay on an identical straight line, which meant that this was the fully elastic deformation stage and two phases showed the same elastic deformation. In all the DP specimens with different grain sizes, stress-partitioning began within the applied stress in the range of 250–300 MPa, demonstrating that this phenomenon occurs prior to macroscopic yielding (0.2 % proof stress; 378 MPa for CG, 510 MPa for MG, and 501 MPa for FG specimens). After the initiation of stress-partitioning, ferrite had lower phase stress than martensite. This indicated that the plastically softer ferrite phase took more plastic deformation while the plastically harder martensite born more elastic deformation, which agreed with the result of strain-partitioning (Fig. 6). The degree of stress-partitioning increased with the progress of plastic deformation of the specimens. Compared at a same applied stress, the degree of stress-partitioning tended to become more pronounced with decreasing the grain size of the DP steel, particularly at the later stages of tensile deformation. The maximum phase stress of martensite in the CG, MG and FG specimens reached 857 MPa, 1101 MPa and 1214 MPa, respectively. The grain refinement had smaller effect on the phase stress of ferrite, with the maximum phase stress values of 474 MPa for CG, 445 MPa for MG and 539 MPa for FG specimens. Such a difference in the

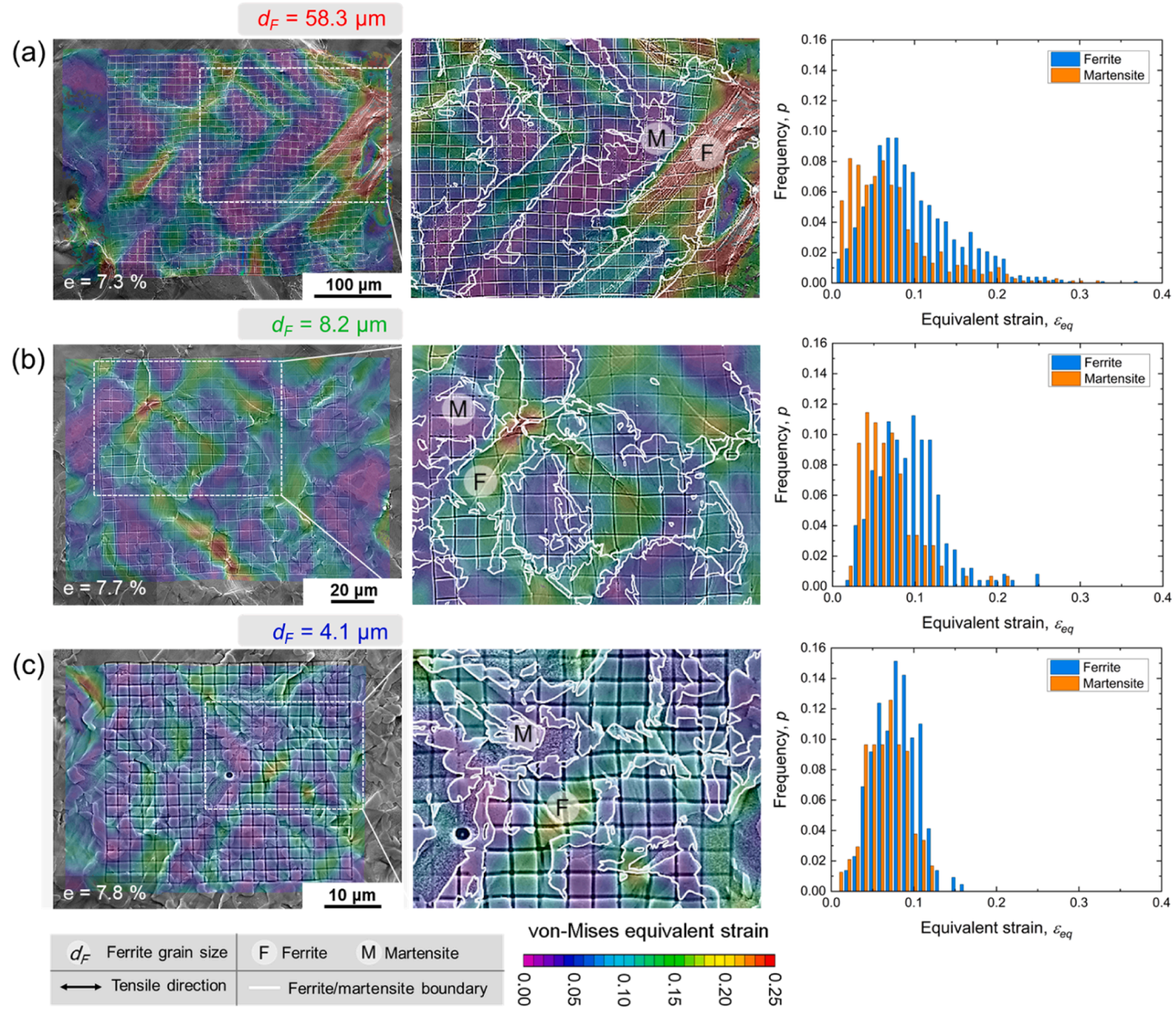

Fig. 5. Local strain distribution overlapped on microstructures (left and middle columns) and histograms showing local strains within either ferrite or martensite phase (right column) obtained by the μ-DIC analysis in the (a) coarse-grained (58.3 μm), (b) medium-grained (8.2 μm), and (c) fine-grained (4.1 μm) DP specimens tensile-deformed to ~7.5 %. The middle column shows enlarged maps of the area surrounded by the white dotted rectangle in the images on the left column. The tensile axis is parallel to the horizontal axis of the images, and the color indicates the value of von-Mises equivalent strain at the position, according to the scale color bar shown at the bottom. In the enlarged maps on the middle column, ferrite/martensite boundaries are marked by white line, and the labels **F** and **M** denote ferrite and martensite regions, respectively.

maximum phase stress (of martensite especially) between DP steel specimens with different grain sizes corresponds to the difference in the strain-hardening ability and the ultimate tensile strength of the DP specimens. This finding is noteworthy because the grain refinement of ferrite eventually enhances the internal stress, i.e., the elastic deformation, of martensite in the DP steel. This suggests that the grain refinement strengthening in the observed DP structure is somehow different from the conventional grain refinement strengthening (Hall-Petch effect) in single-phase metals which is usually explained by dislocation pile-up model at the grain boundary. In the DP steels, or more generally in the metallic materials composed of soft and hard phases/domains, microstructural refinement would lead to enhancing deformation (especially elastic deformation) of the hard phase, resulting in the higher strain, strain-hardening rate and uniform elongation (later plastic instability) of the whole material.

The results of strain-partitioning (Fig. 6) and stress-partitioning (Fig. 9) obtained in the present study could show a clear and reasonable view on the deformation of the DP steels having microstructures composed of soft ferrite and hard martensite. Plastically soft ferrite bears higher plastic strain. However, two phases are connected at their interfaces, so that two phases must deform cooperatively which is the so-called deformation constraint. When ferrite plastically deforms in a larger amount, the deformation constraint forces martensite to deform cooperatively. Because martensite is plastically much harder than ferrite, martensite tries to bear the deformation elastically. This is the reason why martensite showed higher elastic strain (larger peak-shift and lattice strain (Fig. 8(b))). The higher elastic strain in martensite leads to higher internal stress (phase stress), which is one of the important reasons for the enhanced strain-hardening in the DP steel. It is also expected that ferrite has higher dislocation densities leading to larger amount of strain-hardening than the case of single-phase, since ferrite is more plastically deformed than martensite due to the

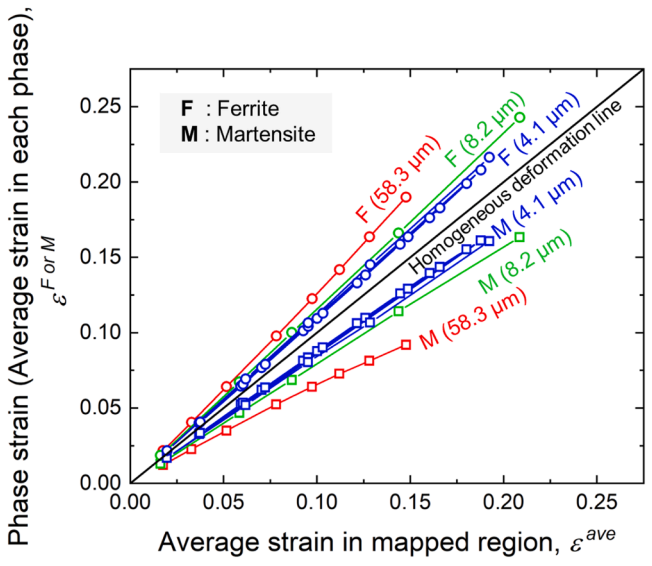

Fig. 6. Results showing strain-partitioning. The average strains in ferrite or martensite phase (phase strain) obtained by the μ-DIC analysis plotted as a function of the average strain of the whole DIC-mapped regions. The data cover a wide global tensile strain range: from 0 % to 11.8 % for the CG specimen, 15.2 % for the MG specimen, and 15.3 % for the FG specimen. Within the uniform elongation range (approximately 9 % engineering strain), the average strains of the whole mapped regions matched well with the global tensile strain of the specimen. The black straight line represents homogeneous deformation when the phase strain is equal to the average global strain.

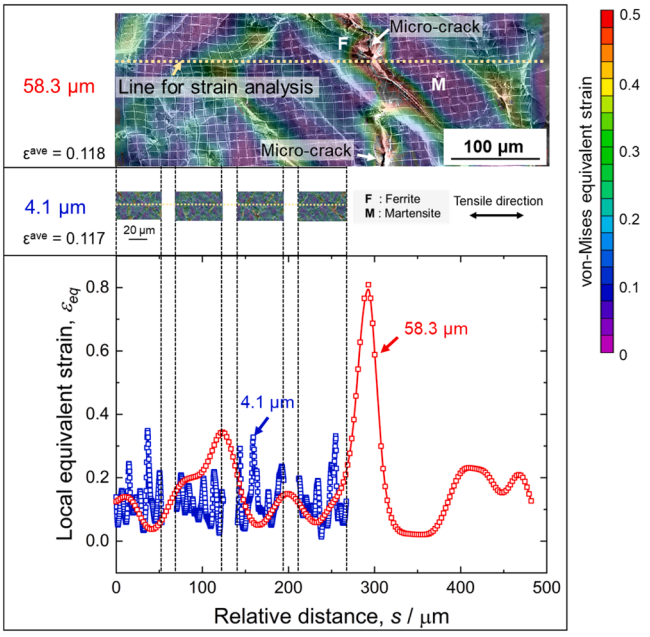

Fig. 7. Results of μ-DIC analysis for the CG (58.3 μm) and FG (4.1 μm) specimens of the DP steel tensile deformed to a tensile engineering strain of about 12 %. Upper image: Local strain map of the CG specimen overlapped on the microstructure. **F** and **M** indicate ferrite and martensite phases, respectively. Micro-cracks observed are pointed by the white arrows. Middle images: Local strain maps of the FG specimen overlapped on the microstructure. Lower graph: Local strain profiles along the yellow dotted lines in the local strain maps of the CG and FG specimen, plotted as a function of the distance in the same scale. Red and blue curves correspond to the local strain profiles of the CG and FG specimens, respectively (For interpretation of the references to colour in this figure legend, the reader is referred to the web version of this article.).

deformation constraint. Additionally, it was found in the present study that the microstructural refinement of DP steels made plastic deformation in two phase more homogeneous (Fig. 6). As a result, hard martensite could be more deformed plastically in the finer DP structure and would probably have higher dislocation density. Such increases in dislocation densities in ferrite and martensite might also contribute to the enhanced strain-hardening (i.e., both of high strength and high ductility (uniform elongation)) of the FG specimen. Then, let us consider why the grain refinement of ferrite enhances the phase stress and plastic deformation of martensite (Fig. 9).

Fig. 10 shows the (a) fraction and (b) density of ferrite/martensite (F/M) and ferrite/ferrite (F/F) boundaries evaluated from SEM microstructure in the present DP steels having different ferrite grain sizes. For simplicity, martensite/martensite boundaries were not taken into account in this study due to the complex microstructural features of martensite including various substructures, such as, laths, blocks, packets and their boundaries. The density was calculated as the total length of boundaries per unit area of the observed microstructure, with a unit of $[\mu m/\mu m^2] = [\mu m^{-1}]$, assuming this is equal to the total boundary area per unit volume ($[\mu m^2/\mu m^3] = [\mu m^{-1}]$). The fraction of F/M boundaries is overwhelmingly higher than that of F/F boundaries in all the DP specimens used in the present study, and the density of F/M boundaries greatly increased with the grain refinement. Again, deformation of two phases (ferrite and martensite) having different mechanical properties is constrained at their interfaces (F/M boundaries in Fig. 10). The microstructural refinement of the DP steel naturally increased the density of F/M boundaries, so that increased constraint positions in the material. Assuming that the distribution of elastic strain within martensite is not homogeneous but higher near the F/M boundary (constraint position), total amount of elastic strain borne in martensite would increase. This could be the reason why the grain refinement of ferrite in the DP steel enhanced the phase stress in martensite (Fig. 9), which was one of the reasons for the enhanced strain-hardening and uniform elongation (postponement of plastic instability) in the DP specimens with finer ferrite grain size. The increase of the F/M boundary density would also homogenize plastic deformation within the whole DP material, which has been experimentally shown in Figs. 6 and 7. Such homogenization of deformation in the whole material suppressed crack initiation, which must be one of the reasons for the increased ductility in the DP steel by the microstructure refinement. Also, the enhanced plastic deformation would lead to the increase of dislocation densities in ferrite and martensite, which could be another reason for the enhanced strain-hardening. It should be also noted that the present DP specimens had the morphology where martensite surrounds isolated ferrite. In such a chained martensite morphology, the density of F/M boundaries is maximized, which coincides well with the reported facts that the DP steels having chained martensite morphology show good strength-ductility balance compared with other morphologies [1–3].

3.5. *Reconstruction of individual tensile properties in ferrite and martensite*

Finally, we attempt to combine the acquired strain- and stress-partitioning results to reconstruct the individual tensile properties of ferrite and martensite in the DP steel, which has never been realized experimentally. Fig. 11(a) illustrates the method to reconstruct the stress-strain curve of ferrite and martensite separately. Each arbitrary point on the global stress-strain (S-S) curve can be subdivided into two S-S points for each phase as follows: The DIC strain results provide the average strain of each phase (ε_1^F, ε_1^M) at the given global strain (ε_1), while the *in-situ* neutron diffraction results provide the average stress of each phase (σ_1^F, σ_1^M; phase stress) at the given global stress (σ_1). By applying this method to different points till the uniform elongation, true S-S curves for each phase could be successfully reconstructed, as shown in Fig. 11(b). Average strain of ferrite or martensite was evaluated from the

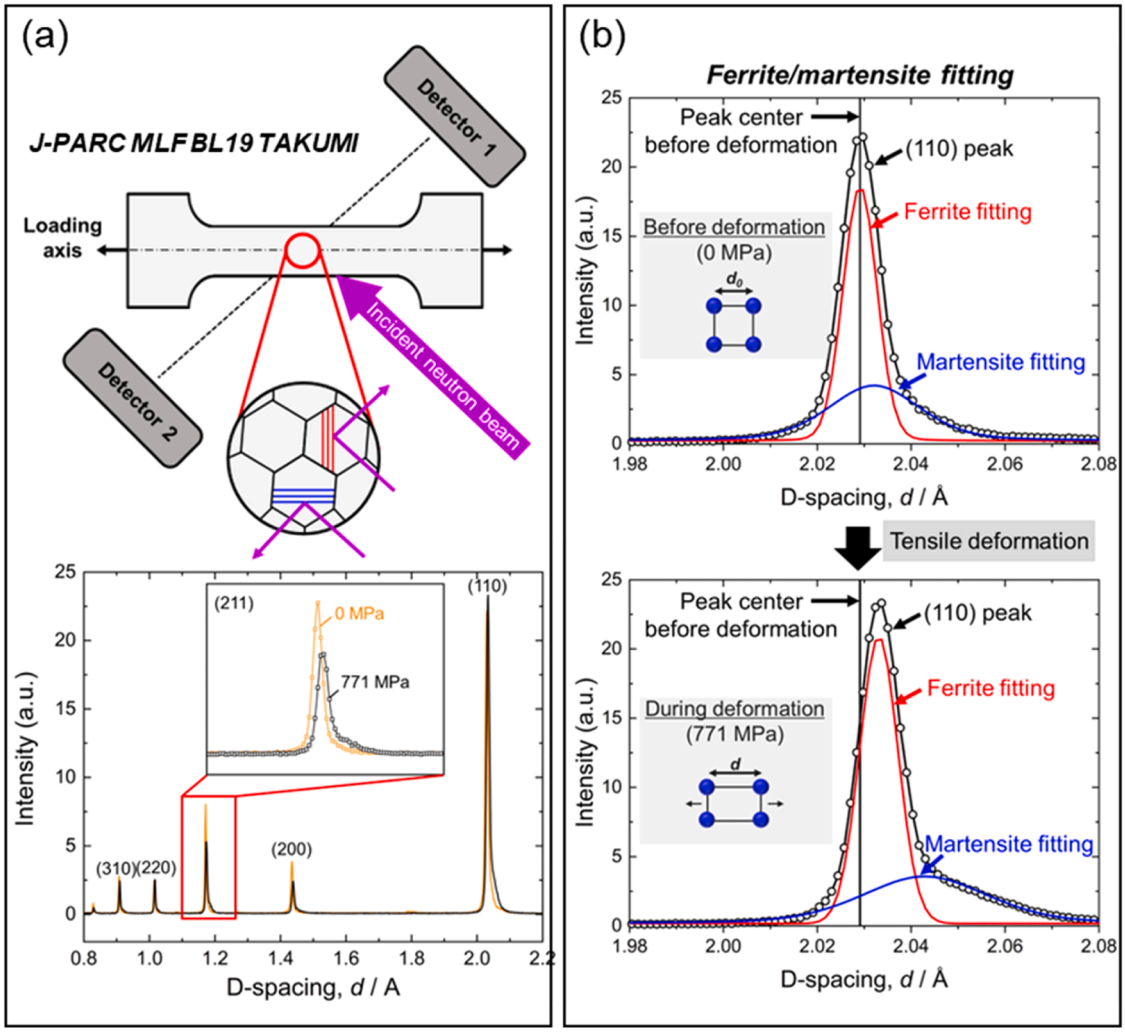

Fig. 8. *In-situ* neutron diffraction for analyzing the evolution of internal stress in ferrite and martensite during tensile deformation. (a) Schematic illustration of the *in-situ* neutron diffraction experiment performed at J-PARC (Japan Proton Accelerator Research Complex) MLF (Materials and Life Science Experimental Facility) Beam line-19 TAKUMI. The experimental setup involving a specific angle alignment between the incident neutron beam, tensile axis, and two detectors, which enables measurement of changes in (hkl) d-spacing perpendicular or parallel to the tensile axis. Lower figure shows an actual examples of diffraction peak profiles before and during tensile deformation with external stress of 0 MPa and 771 MPa, respectively, in the fine-grained (FG) specimen with an average ferrite grain size of 4.1 μm. (b) Enlarged diffraction peak profiles of (110) planes before (0 MPa) and during (771 MPa) tensile deformation in the FG specimen. Diffraction peaks of (110) planes perpendicular to the tensile axis, detected by the detector 1 in (a), are exhibited. Peak fitting analysis is applied on the (110) peaks to separate into two different peaks of ferrite and martensite.

μ-DIC result of the DP specimen of which microstructure was a mixture of ferrite and martensite and of which deformation was cooperatively done. Average phase (internal) stress of ferrite and martensite was evaluated from the shift of the center position of the broadened diffraction peak for each phase, and the neutron diffraction data of the DP steel involved the effect of constraint between two different phases. It is important to note that each reconstructed S-S curve does not represent the pure tensile properties of individual phases, but rather the properties of each phase in the ferrite-martensite mixture state. Namely, this does not imply that the martensite itself becomes stronger due to grain refinement. Rather, it would be more reasonable to consider that a large fraction of martensite, particularly near the interfacial boundaries, actively contributes to the overall deformation, leading to higher apparent internal stress in martensite. Therefore, the resultant increase in internal stress reflects the enhanced role of martensite in accommodating plastic deformation, rather than a direct increase in the intrinsic strength of martensite. In Fig. 11(b), the circle symbol on each curve represents the S-S condition of ferrite, martensite, and the original DP specimen at a global strain of 5 %. The three-point set, consisting of points on ferrite, martensite, and original DP curves for each specimen, lies on a single straight line. This indicates that the linear rule-of-mixture is satisfied for both strain ($\varepsilon = f^F\varepsilon^F + f^M\varepsilon^M$) and stress ($\sigma = f^F\sigma^F + f^M\sigma^M$), where **f** denotes volume fraction, and superscripts **F** and **M** indicate ferrite and martensite, respectively. With the grain refinement (i.e., microstructure refinement), the tie-line at the engineering strain of 5 % became vertically aligned, indicating more homogeneous deformation between ferrite and martensite. The tensile curves for individual ferrite and martensite showed typical flow stress behavior usually observed in metals, characterized by continuous yielding, followed by strain-hardening during tensile deformation. Grain refinement of the DP steel enhanced the strength of both phases, and significantly improved the flow stress of martensite. Martensite displayed a superior strain-hardening ability, which was greatly enhanced by the grain refinement, which resulted from the enhanced elastic and plastic deformation of martensite owing to the increase of the deformation constraint, as was discussed in the former section.

To further validate the reconstructed stress levels in martensite, we analyzed the influence of carbon concentration, which plays a key role

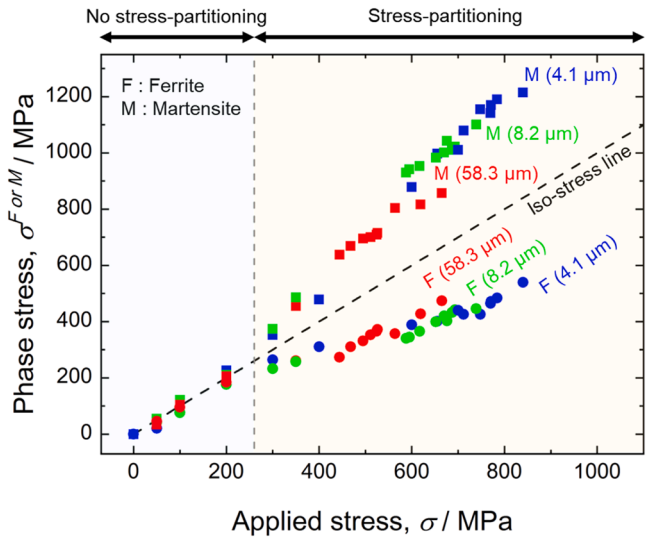

Fig. 9. Stress-partitioning results acquired from the *in-situ* neutron diffraction experiments during tensile deformation. The changes in the phase stress (internal (elastic) stress) borne by each phase) for ferrite (F) and martensite (M) plotted as a function of the external applied stress in the tensile deformation. The data were plotted till the global uniform elongation of each specimen. The black broken line represents the isostress line between the external applied stress and the phase stress.

in determining the hardness and strength of martensite. The carbon concentration of martensite in DP structures can be simply estimated using rule-of-mixture: $C_m=(C_c-C_f(1-f_m))/f_m$, where C_c is the average carbon concentration of the alloy, C_f and C_m are the carbon concentration for ferrite and martensite, respectively [6,28,29]. f_m is the martensite fraction. Considering the limited solubility of carbon in ferrite, it would be reasonable to assume $C_f \sim 0$ [29]. Under this assumption, the equation simplifies to a function martensite fraction alone: $C_m \sim C_c/f_m$. This method, while simple, provides a useful estimation for the upper bound of carbon concentration in martensite. Considering the martensite volume fraction is 0.43, the estimated carbon concentration in martensite is approximately 0.24 (wt. %). Mn partitioning was not considered in this estimation. Although the tensile properties of a fully martensitic structure with the estimated chemical composition (Fe-2Mn-0.24C) were not investigated, those for both Fe-2Mn-0.1C (our result for reference, shown in Fig. S4) and Fe-3Mn-0.2C (Okada et al. [30]) have been investigated. The martensitic structure with Fe-2Mn-0.1C exhibited a yield strength (0.2 % offset stress) of 886 MPa and ultimate tensile strength (UTS) of 1183 MPa. The yield strength and UTS for the Fe-3Mn-0.2C martensitic structure were 1032 MPa and approximately 1500 MPa, respectively. Our reconstructed yield strengths in martensite for CG, MG and FG specimens were 733 MPa, 883 MPa and 944 MPa, respectively, with corresponding UTS values (from engineering stress-strain curves) of 908 MPa, 1126 MPa and 1299 MPa, respectively. The reconstructed stress levels in the FG specimen are positioned between those of Fe-2Mn-0.1C and Fe-3Mn-0.2C martensitic structures. However, those in the MG and CG specimens exhibit lower yield strength and UTS than the Fe-2Mn-0.1C fully martensitic structure. This discrepancy may reflect differences in the degree of deformation contribution by martensite, but further investigation is required to clarify this effect.

While this estimation validates stress levels in the reconstructed S-S curve for martensite, the phase mixture effect implies that the tensile behavior of martensite in DP steels does not need to perfectly match that of pure martensitic structures, even if the chemical composition is identical. This is because the mechanical properties of martensite in DP steels are influenced not only by its chemical composition but also by the interaction with the surrounding ferrite matrix and the constraint effect arising from the interfacial boundaries.

In order to explore the strain-hardening behavior of each phase clearly, the strain-hardening rate ($d\sigma^F/d\varepsilon^F$ or $d\sigma^M/d\varepsilon^M$) curves of two phases were obtained by differentiating the reconstructed true S-S curves. Fig. 11(c) shows the obtained strain-hardening rate curves of ferrite (left-hand side) and martensite (right-hand side), together with the corresponding true S-S curves. In Fig. 11(c), the crossing points of the strain-hardening rate curve and true S-S curve are indicated by the square symbol, and an enlarged view of the yellow-colored region (i) or (ii) is inserted in the graphs. The strain-hardening rate curves for ferrite and martensite exhibited a monotonous decrease with tensile deformation, but the decreasing rate for ferrite was more gradual than that for martensite. In ferrite, the finer grain-sized specimen showed somehow higher strain-hardening rate than the coarser grain-sized specimen up to a true strain of 0.025. After the true strain of 0.025, all the specimens exhibited nearly identical strain-hardening rates of ferrite. On the other hand, martensite in the FG specimen exhibited higher strain-hardening rate than those in the MG and CG specimens throughout the deformation, which obviously correspond to the higher phase stress in martensite in the finer grain-sized specimen. Notably, the decrease in the strain-hardening rate of martensite became significantly more gradual after a true strain of 0.04 in the DP specimen with finer

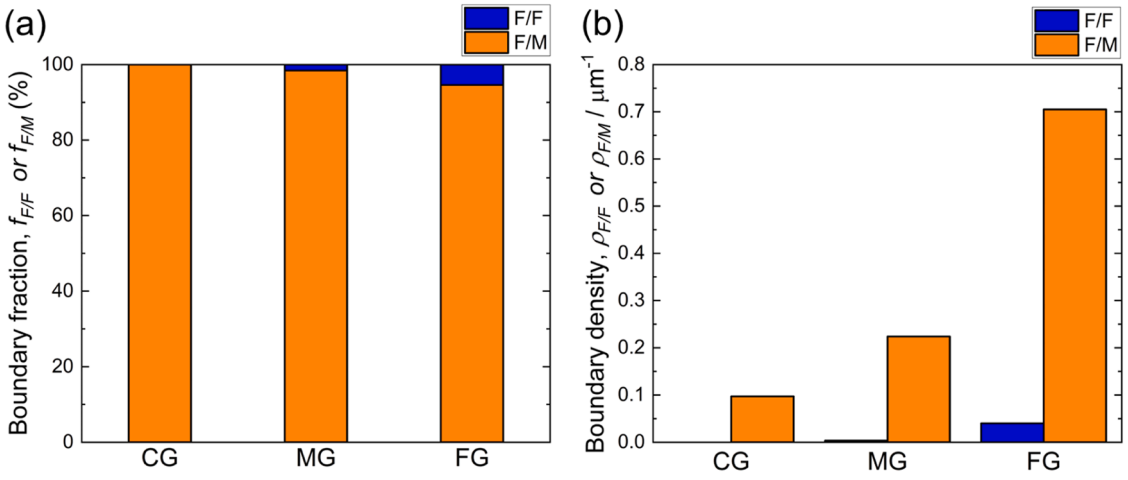

Fig. 10. Boundary characterization in the DP specimens with a grain size of 58.3 μm (CG), 8.2 μm (MG) and 4.1 μm (FG). (a) Boundary fractions and (b) boundary densities of ferrite/ferrite (F/F) boundaries (blue) and ferrite/martensite (F/M) boundaries (orange) (For interpretation of the references to colour in this figure legend, the reader is referred to the web version of this article.).

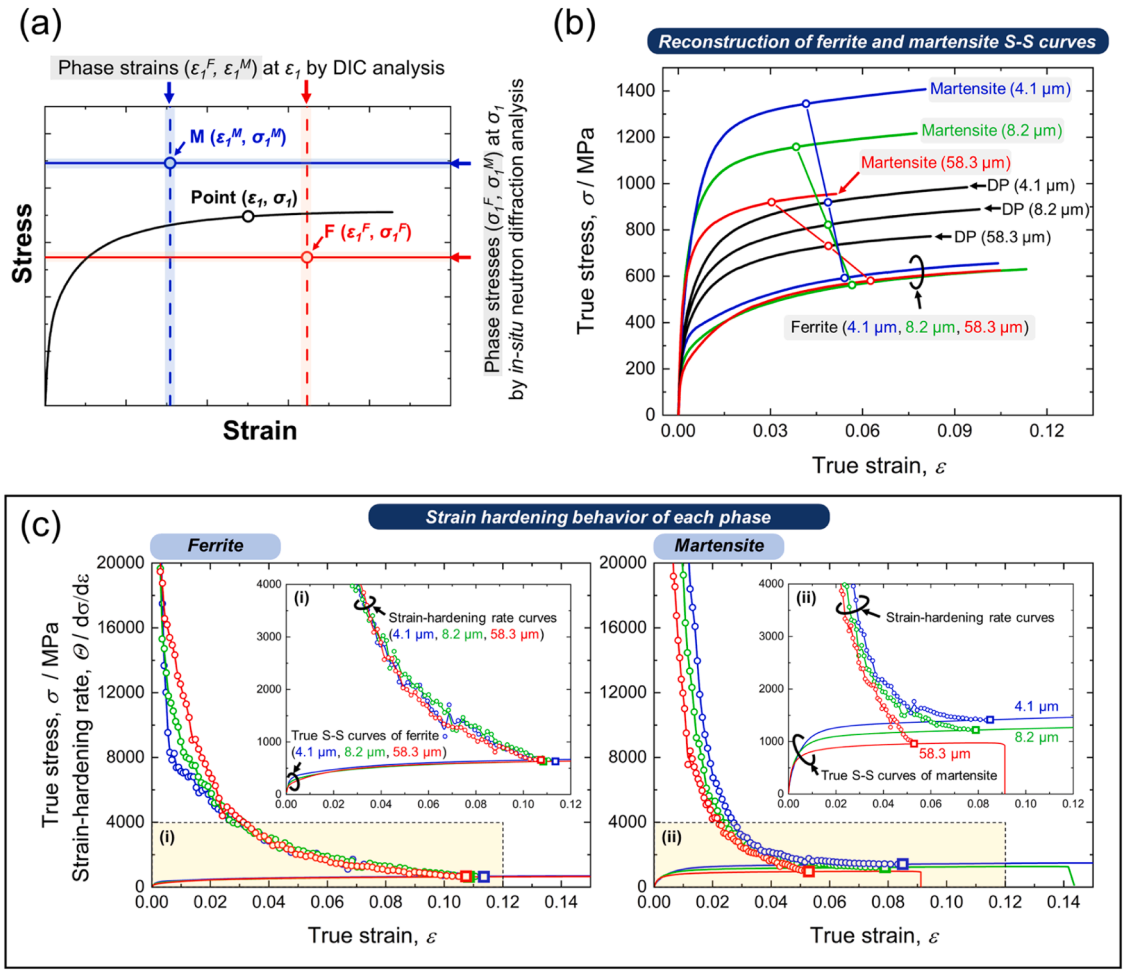

Fig. 11. Reconstruction of stress-strain curves of two phases (ferrite and martensite), realized from the phase strain obtained by the μ-DIC analysis (Fig. 6) and the phase stress by the *in-situ* neutron experiments (Fig. 8). (a) Schematic illustration showing how to reconstruct the stress-strain curves of each phase from the average strain and stress in two phases obtained at a given global stress. By combining such data points at different tensile deformation, the individual stress-strain curves of two phases in the DP microstructures were acquired. (b) Reconstructed stress-strain curves of ferrite and martensite together with that of the whole DP specimen. The circle symbols indicate individual stress-strain points for ferrite, martensite, and the points at tensile strain of 5 % on the original DP curves in the DP structures having three different average ferrite grain sizes. (c) Strain-hardening rate curves for ferrite (left) and martensite (right) in the CG, MG and FG specimens of the DP steel, obtained by differentiating the reconstructed true stress-strain curves. The crossing point of the strain-hardening curve and the stress-strain curve are represented by the square symbols and corresponds to the plastic instability point. The yellow-colored areas for (i) ferrite or (ii) martensite region are enlarged in the graphs (For interpretation of the references to colour in this figure legend, the reader is referred to the web version of this article.).

microstructure, thereby delaying the plastic instability point. The results indicate that martensite plays a crucial role in demonstrating the high strength, outstanding strain-hardening ability and larger uniform elongation of the DP structures. More importantly, the role of martensite as a strain-hardening booster becomes more pronounced with the microstructure refinement. From the results shown in Fig. 11, the reconstruction of stress-strain behavior of each phase in DP structures proposed for the first time in the present study could deepen the discussion on the global deformation behavior of DP steels, as well as provide deeper insight into the individual deformation characteristics of each phase in DP microstructures.

The present study has quantitatively investigated the deformation role of ferrite and martensite in the DP steel based on the acquired results of strain- and stress-partitioning. Grain refinement in DP structures plays an important role by increasing the deformation constraint sites, i.e., ferrite/martensite interfaces, which maximizes the deformation ability of martensite. The microstructural refinement in the DP steel makes the deformation of two phases (soft ferrite and hard martensite) more homogeneous. The resultant larger plastic deformation in martensite in the finer DP microstructure can release strain localization in ferrite, leading to avoiding fracture. Another key finding is the significant increase in the internal stress of martensite by the grain refinement, which enhances the overall strain-hardening ability of the DP structure. The current study reveals that the direct contribution of conventional grain refinement strengthening in ferrite is rather minor but the primary factor driving the improved strength and ductility in the fine DP structures is the deformation constraint effect at ferrite/martensite interfaces that could greatly facilitate the deformation of martensite. The conclusion obtained in the present study, i.e., "the grain refinement in DP structures can well overcome the strength-ductility trade-off dilemma", provides valuable insights into general material design strategies for hetero-structured materials composed of soft and hard domains aiming to manage both high strength and large ductility.

4. Conclusions

In the present study, the mechanical property and local deformation behavior of the ferrite-martensite dual-phase (DP) steel having network-morphology of martensite surrounding ferrite with different average grain sizes were systematically analyzed using the digital image correlation (DIC) analysis and the *in-situ* neutron diffraction experiment during tensile deformation. The main conclusions are summarized as

follows:

(1) Ferrite-martensite DP structures with net-work morphology of martensite surrounding ferrite having average grain sizes of 58.3 μm (coarse-grained, CG), 8.2 μm (medium-grained, MG), and 4.1 μm (fine-grain size, FG) were successfully fabricated through originally designed heat treatments. The fractions of martensite were similar (~43 %) and nano-indentation measurements confirmed that martensite consistently had higher hardness than ferrite, with no significant grain size dependence in hardness observed for either phase.
(2) The grain refinement of the DP structure significantly enhanced both strength and ductility in tensile deformation at room temperature, particularly improving post-uniform elongation. The specimen-scale DIC-strain distribution analysis clearly revealed that the fine-grained DP specimen having the fine average ferrite grain size of 4.1 μm effectively delayed necking progression in necked regions, leading to greater post-uniform elongation.
(3) The μ-DIC analysis showed that, as the average ferrite grain size decreased, deformation became more homogeneous in the DP microstructures, i.e., the hard martensite came to bear more plastic strain, which indicated that the increase in the deformation constraint (owing to the increase in the ferrite/martensite interfaces) maximized the deformation ability of martensite. The deformation homogenization led to decreasing strain localization and crack initiation in ferrite, which explains the improved tensile ductility in the DP steels with finer microstructures.
(4) Martensite bore higher phase stress (internal elastic stress) than ferrite during deformation of DP steel, and the microstructure refinement significantly increased the internal stress of martensite due to the deformation constraint by the increased ferrite/martensite interfaces. The increased phase stress in martensite enhanced the strain-hardening rate and then postponed initiation of the plastic instability in the fine grain-sized DP steel.
(5) The results on the DP steel obtained in the current study gives valuable insights into general strategies for designing hetero-structured materials composed of soft and hard domains aiming to manage both high strength and large ductility.

CRediT authorship contribution statement

Myeong-heom Park: Writing – review & editing, Writing – original draft, Visualization, Methodology, Investigation, Formal analysis, Conceptualization. **Akinobu Shibata:** Writing – review & editing, Investigation, Formal analysis. **Stefanus Harjo:** Resources, Methodology. **Nobuhiro Tsuji:** Writing – review & editing, Validation, Supervision, Funding acquisition.

Declaration of interests

The authors declare no competing interests.

Acknowledgments

This research work was financially supported by the Elements Strategy Initiative for Structural Materials (ESISM; JPMXP0112101000), JST CREST for Nano-Mechanics (JPMJCR1994), and KAKENHI (Grant-in-Aid for Scientific Research from the Japan Society for the Promotion of Science; JP22K18888, JP23H00234, JP23K20037, JP20K14608 and JP24K07214), all from the Ministry of Education, Culture, Sports, Science and Technology (MEXT), Japan. The main result of the present work was performed at Kyoto University, Japan in M-H P's Ph.D. course. We sincerely thank Dr. Toshiro Okawa and Dr. Ian Thomas Clark of Scienta Omicron, Inc. for their technical support with the nano-indentation measurements. The neutron experiment at the Materials and Life Science Experimental Facility (MLF) of J-PARC was conducted under a user program (Proposal No. 2018B0150). All the supports are gratefully appreciated.

Supplementary materials

Supplementary material associated with this article can be found, in the online version, at doi:10.1016/j.actamat.2025.121061.

References

[1] D. Terada, G. Ikeda, M.-h. Park, A. Shibata, N. Tsuji, Reason for high strength and good ductility in dual phase steels composed of soft ferrite and hard martensite, IOP Conf. Ser. Mater. Sci. Eng. (2017), https://doi.org/10.1088/1757-899X/219/1/012008.
[2] K. Park, M. Nishiyama, N. Nakada, T. Tsuchiyama, S. Takaki, Effect of the martensite distribution on the strain hardening and ductile fracture behaviors in dual-phase steel, Mater. Sci. Eng. A. 604 (2014) 135–141, https://doi.org/10.1016/j.msea.2014.02.058.
[3] M.-h. Park, R. Matsubayashi, A. Shibata, N. Tsuji, Quantitative characterization of local deformation-fracture behavior in ferrite-martensite dual-phase steels with different martensite distributions, Mater. Sci. Eng. A. 918 (2024) 147445, https://doi.org/10.1016/j.msea.2024.147445.
[4] M. Calcagnotto, D. Ponge, D. Raabe, Effect of grain refinement to 1μm on strength and toughness of dual-phase steels, Mater. Sci. Eng. A. 527 (2010) 7832–7840, https://doi.org/10.1016/j.msea.2010.08.062.
[5] B. Gao, R. Hu, Z. Pan, X. Chen, Y. Liu, L. Xiao, Y. Cao, Y. Li, Q. Lai, H. Zhou, Strengthening and ductilization of laminate dual-phase steels with high martensite content, J. Mater. Sci. Technol. 65 (2021) 29–37, https://doi.org/10.1016/j.jmst.2020.03.083.
[6] M. Calcagnotto, Y. Adachi, D. Ponge, D. Raabe, Deformation and fracture mechanisms in fine- and ultrafine-grained ferrite/martensite dual-phase steels and the effect of aging, Acta Mater. 59 (2011) 658–670, https://doi.org/10.1016/j.actamat.2010.10.002.
[7] N. Saeidi, F. Ashrafizadeh, B. Niroumand, Development of a new ultrafine grained dual phase steel and examination of the effect of grain size on tensile deformation behavior, Mater. Sci. Eng. A. 599 (2014) 145–149, https://doi.org/10.1016/j.msea.2014.01.053.
[8] W. Bednarczyk, M. Wątroba, G. Cieślak, M. Ciemiorek, K. Hamułka, C. Schreiner, R. Figi, M. Marciszko-Wiąckowska, G. Cios, J. Schwiedrzik, J. Michler, N. Gao, M. Lewandowska, T.G. Langdon, Enhanced mechanical properties and microstructural stability of ultrafine-grained biodegradable Zn–Li–Mn–Mg–Cu alloys produced by rapid solidification and high-pressure torsion, Mater. Sci. Eng. A. 892 (2024) 146027, https://doi.org/10.1016/j.msea.2023.146027.
[9] N. Tsuji, Y. Ito, Y. Saito, Y. Minamino, Strength and ductility of ultrafine grained aluminum and iron produced by ARB and annealing, Scr. Mater. (2002), https://doi.org/10.1016/S1359-6462(02)00282-8.
[10] N. Kamikawa, N. Tsuji, Microstructure and mechanical properties of ARB processed aluminium with different purities, Mater. Trans. 57 (2016) 1720–1728, https://doi.org/10.2320/matertrans.MH201519.
[11] A. Azushima, R. Kopp, A. Korhonen, D.Y. Yang, F. Micari, G.D. Lahoti, P. Groche, J. Yanagimoto, N. Tsuji, A. Rosochowski, A. Yanagida, Severe plastic deformation (SPD) processes for metals, CIRP Ann. - Manuf. Technol. 57 (2008) 716–735, https://doi.org/10.1016/j.cirp.2008.09.005.
[12] N. Tsuji, R. Gholizadeh, R. Ueji, N. Kamikawa, L. Zhao, Y. Tian, Y. Bai, A. Shibata, Formation mechanism of ultrafine grained microstructures: various possibilities for fabricating bulk nanostructured metals and alloys, Mater. Trans. 60 (2019) 1518–1532, https://doi.org/10.2320/matertrans.MF201936.
[13] N. Tsuji, S. Ogata, H. Inui, I. Tanaka, K. Kishida, S. Gao, W. Mao, Y. Bai, R. Zheng, J.P. Du, Strategy for managing both high strength and large ductility in structural materials–sequential nucleation of different deformation modes based on a concept of plaston, Scr. Mater. 181 (2020) 35–42, https://doi.org/10.1016/j.scriptamat.2020.02.001.
[14] C.C. Tasan, J.P.M. Hoefnagels, M. Diehl, D. Yan, F. Roters, D. Raabe, Strain localization and damage in dual phase steels investigated by coupled in-situ deformation experiments and crystal plasticity simulations, Int. J. Plast. 63 (2014) 198–210, https://doi.org/10.1016/j.ijplas.2014.06.004.
[15] S.H. Joo, J.K. Lee, J.M. Koo, S. Lee, D.W. Suh, H.S. Kim, Method for measuring nanoscale local strain in a dual phase steel using digital image correlation with nanodot patterns, Scr. Mater. 68 (2013) 245–248, https://doi.org/10.1016/j.scriptamat.2012.10.025.
[16] W. Mao, S. Gao, W. Gong, Y. Bai, S. Harjo, M.H. Park, A. Shibata, N. Tsuji, Quantitatively evaluating respective contribution of austenite and deformation-induced martensite to flow stress, plastic strain, and strain hardening rate in tensile deformed TRIP steel, Acta Mater. 256 (2023) 119139, https://doi.org/10.1016/j.actamat.2023.119139.
[17] M.-h. Park, Y. Fujimura, A. Shibata, N. Tsuji, Effect of martensite hardness on mechanical properties and stress /strain-partitioning behavior in ferrite + martensite dual-phase steels, Mater. Sci. Eng. A. 916 (2024) 147301, https://doi.org/10.1016/j.msea.2024.147301.
[18] R.A. Grange, The rapid heat treatment of steel, Metall. Trans. 2 (1971) 65–78.

[19] T. Furuhara, K. Kikumoto, H. Saito, T. Sekine, T. Ogawa, S. Morito, T. Maki, Phase transformation from fine-grained austenite, ISIJ Int. (2008), https://doi.org/10.2355/isijinternational.48.1038.
[20] M.-h. Park, A. Shibata, N. Tsuji, Challenging ultra grain refinement of ferrite in low-C steel only by heat treatment, Front. Mater. 7 (2020) 1–10, https://doi.org/10.3389/fmats.2020.604792.
[21] Y. Tomota, P. Lukáš, D. Neov, S. Harjo, Y.R. Abe, In situ neutron diffraction during tensile deformation of a ferrite-cementite steel, Acta Mater. 51 (2003) 805–817, https://doi.org/10.1016/S1359-6454(02)00472-X.
[22] S. Morito, H. Yoshida, T. Maki, X. Huang, Effect of block size on the strength of lath martensite in low carbon steels, Mater. Sci. Eng. A. 438–440 (2006) 237–240, https://doi.org/10.1016/j.msea.2005.12.048.
[23] A. Shibata, T. Nagoshi, M. Sone, S. Morito, Y. Higo, Evaluation of the block boundary and sub-block boundary strengths of ferrous lath martensite using a micro-bending test, Mater. Sci. Eng. A. 527 (2010) 7538–7544, https://doi.org/10.1016/j.msea.2010.08.026.
[24] T. Kaneshita, G. Miyamoto, T. Furuhara, Variant selection in grain boundary nucleation of bainite in Fe-2Mn-C alloys, Acta Mater. 127 (2017) 368–378, https://doi.org/10.1016/j.actamat.2017.01.035.
[25] A. Considère, Ann. Ponts Chaussees 9 (1885) 574775.
[26] G.V. Kurdjumov, Martensite crystal lattice, mechanism of austenite-martensite transformation and behavior of carbon atoms in martensite, Metall. Trans. A 7 (1976) 999–1011.
[27] D. Fukui, N. Nakada, S. Onaka, Internal residual stress originated from Bain strain and its effect on hardness in Fe–Ni martensite, Acta Mater. 196 (2020) 660–668, https://doi.org/10.1016/j.actamat.2020.07.013.
[28] Y. Mazaheri, A. Kermanpur, A. Najafizadeh, Nanoindentation study of ferrite-martensite dual phase steels developed by a new thermomechanical processing, Mater. Sci. Eng. A. 639 (2015) 8–14, https://doi.org/10.1016/j.msea.2015.04.098.
[29] S.S. Ghasemi Banadkouki, E. Fereiduni, Effect of prior austenite carbon partitioning on martensite hardening variation in a low alloy ferrite-martensite dual phase steel, Mater. Sci. Eng. A. 619 (2014) 129–136, https://doi.org/10.1016/j.msea.2014.09.041.
[30] K. Okada, A. Shibata, T. Sasaki, H. Matsumiya, K. Hono, N. Tsuji, Improvement of resistance against hydrogen embrittlement by controlling carbon segregation at prior austenite grain boundary in 3Mn-0.2C martensitic steels, Scr. Mater. 224 (2023) 115043, https://doi.org/10.1016/j.scriptamat.2022.115043.